

On the opportunities and challenges provided by mask-based x-ray micro-CT



Amy Quynh Ha

Department of Medical Physics and Biomedical Engineering

University College London

A thesis submitted for the degree of

Master of Philosophy

November 2022

I, Amy Quynh Ha confirm that the work presented in this thesis is my own. Where information has been derived from other sources, I confirm that this has been indicated in the thesis.

Abstract

Edge Illumination (EI) is one of several X-ray Phase Contrast Imaging (XPCI) techniques capable of providing multi-modal images, revealing structures in objects that can be difficult to image using the conventional, absorption-based x-ray method. The EI method is underpinned by the use of masks in the scanner, one to split the beam into an array of beamlets, and another one to create sharp edges in front of a pixelated detector.

The study presented in this thesis explores the pros and cons of using those masks. In the main chapter, computed tomography (CT) scans were taken of a wooden pencil using an x-ray imaging setup without masks, one mask, and two masks. It was verified that the use of one and two masks increases the spatial resolution and CNR, respectively, compared to a mask-less approach. However, a major drawback associated with the use of masks are that scan times are typically long. In this context, this thesis discusses recently developed approaches to facilitate scan time reduction in EI, one being Cycloidal CT – a sampling scheme which aims to improve speed while maintaining high resolution.

Impact Statement

The findings in this thesis provide insight into X-ray Phase Contrast Imaging (XPCI): a research area which extends the contrast capabilities of traditional absorption-based set ups. The work presented here relates to a phase contrast imaging technique, namely Edge-Illumination (EI). The experiment reported in this thesis examines the working principles of the technique – which enables strong contrast, high spatial-resolution images in a laboratory setting. EI is under continuous development, and the results further support Cycloidal CT as a scheme to improve its speed.

Importantly, the potential of translating the technique to real-world environments (owing to its compatibility with standard x-ray tubes) makes it an attractive prospect for a wide breadth of applications, e.g., across the life and physical sciences. Considering a use for medical diagnostic purposes (though application is still somewhat out of reach at present), XPCI may be more desirable from a patient-safety point of view than their traditional counterparts. That is due to better contrast at higher energies, leading to lower dose delivered to patients, and consequently lower risk of cell damage and cancer. In pre-clinical imaging of small animals (such as mice), which is essential when conducting studies on drug development, the better contrast at higher energies may imply a lower dose per scan, which means there can be more extensive longitudinal studies on the same animal (these are typically limited by a certain dose threshold that must not be exceeded).

The ability to acquire tomographic EI images with reduced scan times could ultimately enable its use for high-throughput or dynamic imaging experiments. Moreover, the suggestions made in this thesis could be of relevance to other XPCI techniques, which share similarities with the approach explored here.

Acknowledgements

I would like to pay special thanks to my supervisor Dr. Charlotte K. Hagen, for her kind, patient nature and guidance throughout my journey. This thesis would not have been possible without her invaluable contribution. I would like to express gratitude to those in the Advanced X-ray Imaging group at UCL for sharing their learnings and expertise with me.

Table of Contents

1. Introduction.....	7
1.1 Thesis Aims	9
2. Scientific background.....	10
2.1 Overview of XCPI Techniques.....	10
2.1.1 Bonse-Hart Interferometer.....	11
2.1.2 Free Space Propagation (FSP).....	12
2.1.3 Analyser-based imaging (ABI).....	12
2.1.4 Grating Interferometry (GI).....	13
2.2 Edge-illumination	15
3. Literature review	18
3.1 Multi-modal CT with Edge-illumination	18
3.2 Beam tracking CT	19
3.3 Cycloidal CT	19
4. Project: Altering an imaging system’s resolution and contrast capabilities by means of x-ray absorbing masks	23
4.1 Introduction	23
4.2 Methods	24
4.2.1 Experimental system	24
4.3 Results	27
4.3.1 No masks vs one mask (fully dithered)	27
4.3.2 Two masks (fully dithered)	29
4.3.3 Testing Cycloidal CT on the three contrast channels.....	30
4.4 Discussion	34
5 Conclusion.....	36
Bibliography.....	37

1. Introduction

X-ray Computed Tomography (CT) is a technique that enables the depiction of internal structures at high resolution, such as the human body in diagnostic imaging. Beyond diagnostics, X-ray CT has a broad range of applications such as biomedicine [1] materials science [2], and security scanning [3], to name a few. In those applications, rather than using patient-scale scanners, scans are usually performed with benchtop-scale micro-CT machines. These offer a higher spatial resolution, but typically incur much longer scan times.

The idea behind CT is to take a series of radiographs around an object and use mathematical reconstruction techniques to determine the distribution of the internal properties of the object. It is common to reconstruct 2D “slices” (axial cross sections) through the object, which can be stacked together to form a volumetric representation of the object.

Conventional x-ray CT derives its contrast from the attenuation properties of an object. Images are reconstructed from measurements of transmission, which can be described by the Beer-Lambert law:

$$I(z) = I_0 \cdot e^{-\mu \Delta z} \quad (1)$$

The transmission through the object can be calculated via:

$$T = \frac{I(z)}{I_0} \quad (2)$$

Where $I(z)$ and I_0 are the emerging and incident intensity of a monochromatic wavefield impinging onto the sample material along direction z . μ is the linear attenuation coefficient: the value is material- and energy-dependent, characterising how easily the object can be penetrated by the wave. [4]

In conventional CT, the two- or three-dimensional distribution of μ within a non-uniform object is reconstructed. This is enabled by a line integral relationship between the transmission measurement and the attenuation coefficients within the object. To derive this line integral relationship, it is assumed that the object can be divided into small sections in such a way that each is of uniform μ . The Beer-Lambert law (Eq. 1) now describes the incident and emerging x-ray intensities of each individual section. Considering that an x-ray photon encounters a number of those sections along its path through the object, the Beer-Lambert law can be written as:

$$I = I_0 \cdot e^{-\mu_1 \Delta z} \cdot e^{-\mu_2 \Delta z} \cdot e^{-\mu_3 \Delta z} \dots e^{-\mu_n \Delta z} = I_0 e^{-\lim_{\Delta z \rightarrow \infty} \sum_{n=1}^N \mu_n \Delta z} = I_0 e^{-\int_0^t \mu(z') \cdot dz'} \quad (3)$$

Where t is the thickness of the sample, and the exponent includes the line integral of the attenuation coefficients in the x-ray path. [5]

If we measure the intensity I over an area, for example, with a digital flat panel detector, we obtain a projection of the object, $I(x, y)$. As from Eq. 3, a projection is the integral of the image at a specific angle. In CT, many such projections are acquired as the object is rotated inside the scanner over a range of at least 180 degrees. The set of projections can be ordered into a sinogram, which is a two-dimensional image created for each axial slice in the object, showing how the transmission through each slice varies as a function of the rotation angle. Sinograms can be reconstructed into tomographic slices by applying filtered back projection (FBP). This method, as the name suggests, smears the measurements back across the x-ray trajectory for which they were obtained, but applies a high-pass filter prior to this step to emphasise the higher spatial frequencies that would otherwise be lost due to the repeated averaging involved in the measurement and back projection. Before FBP can be applied, however, the line integral in (3) needs to be isolated, which is achieved by applying the negative logarithm to the transmission measurements.

This conventional, attenuation-based approach to CT provides strong image contrast for large attenuation variation inside an object (for example, between strongly absorbing bone and weakly absorbing soft tissue background); however, contrast may be poor and features indistinguishable for objects composed of only low Z elements such as soft biological tissue, since their intrinsic attenuation is typically weak. [6]

In view of how contrast for those objects may be improved, it is important to note that, when x-rays travel through matter, they are not only attenuated but also undergo a phase shift. Macroscopically, this effect may be described as refraction: x-rays experience a small deviation from their path as they enter and exit materials with a non-trivial refractive index. The value of the x-ray refractive index is very close to unity (a difference on the order of 10^{-6}), with deflections on the scale of a few microradians or less, hence they are difficult to detect. Recent developments in X-ray imaging (and CT) have sought to capitalise on the phase/refraction information to improve image quality for objects that have traditionally been considered difficult to visualise; indeed, a large body of literature has demonstrated that a better contrast for weakly attenuating features can be obtained when phase information is incorporated into the image formation process. From a theoretical point of view, this can be understood by means of the complex refractive index, $n = 1 - \delta - i\beta$, where β is proportional to the linear attenuation coefficient, $\beta = \mu_0 * (\lambda/4\pi)$, and δ is proportional to the phase function $\delta = \phi * (\lambda/2\pi)$, driving refraction. For the hard x-ray range and weakly attenuating materials, δ can be up to three orders of magnitude larger than β , and falls off more slowly with increasing x-ray energy ($1/E$ vs. $1/E^3$). [7] [8] X-ray imaging techniques capable of sensing phase effects are known as “phase contrast” techniques.

Further to phase contrast, it is also possible to detect small-angle (elastic) scattering from the object. Imaging methods capable of doing so are known as “dark-field” or ultra-small angle scattering techniques. The scattering signal is related to sample inhomogeneities: the presence, size, and concentration of features below the resolution of the imaging system, and thus is well suited to studying an object’s microstructure. The interaction responsible for small-angle scattering is the elastic process – coherent scattering. The x-rays are scattered in all directions, according to the Gaussian distribution.

In summary, while initially x-ray imaging and CT had been limited to attenuation-based contrast, nowadays we have up to three contrast channels available: attenuation, refraction and dark-field/scattering. This is known as multi-modal CT.

From an experimental point of view, there are several approaches to realising multi-modal CT. While those will be described in Sec. 2, it should be noted here that phase effects typically cannot be observed directly as is the case for attenuation, but require an elaborate sensing mechanism. The common idea behind the existing experimental approaches is to find a way of converting phase shifts into detectable intensity modulations.

Edge-Illumination (EI) – the technique which is the focus of this MPhil thesis – works by structuring the x-ray beam into an array of narrow, spatially separated beamlets by virtue of a mask placed upstream of the sample, then tracking the beamlets’ attenuation-induced amplitude reduction, refraction-induced shifts, and small angle scattering-induced broadening.

1.1 Thesis Aims

The overarching aim of my MPhil project was to explore mask-based experimental approaches to phase contrast CT; in particular the EI method, which was first demonstrated at the SYRMEP beamline in Trieste, Italy during the late 1990s and has been under continuous development within the AXIm group at UCL.

While in the earlier days, the EI method utilised a synchrotron radiation beam impinging on a single / array of slits which shaped the beam aligned with a detector pixel further down the set-up, more lately it was expanded to laboratory sources by structuring the cone beam emitted from an x-ray tube into an array of beamlets by means of a mask. [9] In this thesis, I will focus on the latter implementation, referred to as mask-based EI.

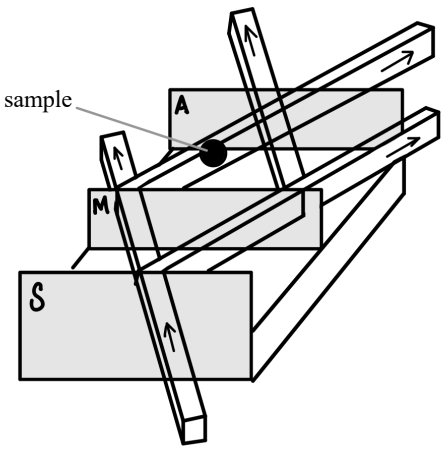
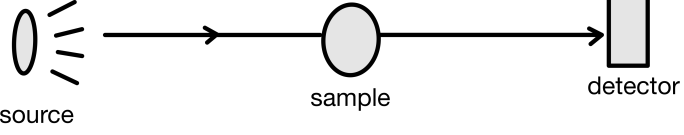
In this work, I will explore the working principle of mask-based EI experimentally. In particular, I will investigate how the addition of either one or two masks in the set-up changes the contrast and spatial resolution capabilities of the imaging system – both of which are key metrics in assessing image quality. While these effects have been demonstrated previously, they were mostly shown as isolated effects. In this thesis, I amalgamate the two, by discussing results from an experiment that shows how the use of masks affects both contrast and spatial resolution.

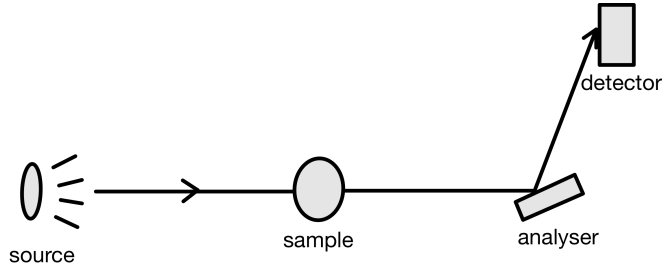
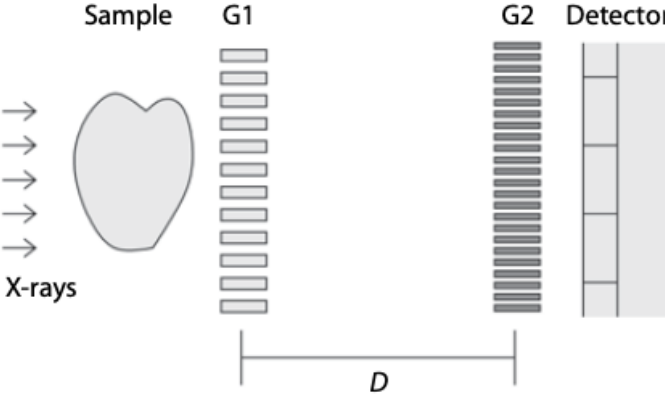
The thesis will begin by providing context to my work in the form of introducing different existing experimental phase contrast approaches in the next section. In Sec. 3, I will provide a Literature Review of the relevant works undertaken within the Advanced X-ray Imaging (AXIm) group at UCL – the team researching the core technology that this thesis relates to. The main project, i.e., the investigation of the mask-based x-ray imaging system, will be presented in Sec. 4. Towards the end of the thesis, I will discuss the benefits and limitations of using such an experimental design. I will also describe some ongoing research aimed at solving the identified limitations.

2. Scientific background

2.1 Overview of XCPI Techniques

Although X-ray Phase Contrast Imaging (XPCI) was proposed in 1965 by Bonse and Hart, multi-modal imaging has only become available for widespread use in recent times as some earlier techniques required beams of high spatial coherence which were only available from synchrotron sources (of which there are only typically one per country, and access is highly restricted). Following nearly a decade of intense development by several groups worldwide, XPCI has been adapted to work with the weakly coherent or incoherent beams emitted from laboratory-type x-ray tubes. In the following, I will provide an overview of existing XPCI techniques, starting from the earliest of the collection and ending with the main topic of this work, namely EI.

XCPI technique	Schematic
Bonse-Hart	 <p data-bbox="558 1400 1380 1512"><i>FIG 1 Schematic of the Bonse-Hart experiment. Comprises of three crystal blades: 'S' – splits the beam into two mutually coherent beams. 'M' – splits the beams again, where two beams recombine. 'A' – helps visualise the interference pattern. A sample in the beam's path will distort the interference pattern</i></p>
Free-space propagation	 <p data-bbox="558 1780 1380 1848"><i>FIG 2 Schematic set-up of free-space propagation. A suitably long distance between the sample and detector allows fringes to form</i></p>

Analyser-based imaging	 <p>FIG 3 Schematic set-up of analyser-based imaging. The analyser crystal converts the refraction induced by the sample into measurable intensity modulations on the detector</p>
Grating interferometry	 <p>FIG 4 Schematic set-up of grating interferometry. At a fractional Talbot distance, the image of grating G1 is replicated. The sample alters the pattern and the differential phase is recorded by scanning the analyser/absorption grating G2. Figure reproduced with permission of the rights holder, Elsevier Ireland Ltd [10]</p>

2.1.1 Bonse-Hart Interferometer

The Bonse-Hart interferometer, as can be seen from Fig. 1, comprises of a perfect crystal block carved to form three parallel thin blades of constant spacing. The three blades act as a beam splitter, mirror, and analyser, respectively. In the original work [11], a copper spectrum was used, and the crystal was silicon 220.

At blade S, the beam is split into two mutually coherent beams by virtue of Laue reflection. Once again, the beams are split at M – two of these are redirected towards each other which produces a standing wave pattern just before A. The x-ray fringes are too small to be detected directly, and the function of the crystal analyser A is to convert them into a detectable intensity pattern. When there is no object in place, periodic interference fringes will be visible at the detector. On the other hand, if an object is placed in one of the paths, then these fringes will be distorted according to the phase shift introduced by the object. A Fourier method can be used to extract the phase shifts to the standing wave pattern. [12]

While the Bonse-Hart method is an extremely sensitive method capable of resolving sub-nanoradian refraction angles, it requires high stability and perfect aligned crystals which may be difficult to achieve in practice as the interferometer is sensitive to small lattice distortions, which was observed in the original paper.

2.1.2 Free Space Propagation (FSP)

FSP has arguably the simplest set-up among the XPCI techniques as it requires only some propagation distance between the sample and detector (see Fig. 2) but is largely the same as a standard radiographic system in all other aspects. The propagation distance allows fringes to form, which result from interference of the distorted (i.e., phase shifted) parts of the wavefront with the non-distorted ones. The intensity fringes are strongest at external and internal boundaries of the scanned object; hence they contribute to a better visualisation and distinction of different object materials and features, especially when these are weakly attenuating. [13]

However, being an interferometric technique, FSP has relatively strict requirements on spatial coherence of the x-rays incident on the sample, which means the x-ray source must be small, or the sample-detector distance must be sufficiently large. For this reason, the method tends to be used at synchrotrons. When applied in the laboratory, it must be implemented with a microfocal x-ray source (early experiments have been conducted by generating an x-ray beam using a scanning electron microscope with source size on the scale of 100nm). [14] However, typically for those sources flux is limited and hence scan times are long.

Alternatively, the recent development of liquid metal-jet x-ray tubes offers an opportunity for significantly reducing scan times in FSP. Rather than using a solid anode to generate x-rays for which x-ray output is limited by the electron beam power at which the anode melts, liquid metal-jet sources utilise an anode in molten state which continuously renews itself (as it is a continuous stream). This allows increasing the x-ray beam power, and consequently provides a much higher x-ray flux, while maintaining a micro-focal spot size. [15] [16] With this new capability, FSP is a real contender for making XPCI a widely used technology. However, it must be noted that contrast in FSP images is limited to attenuation and phase/refraction; the technique is not sensitive to dark-field contrast. Thus, it can only provide bi-modal rather than tri-modal information.

2.1.3 Analyser-based imaging (ABI)

The three contrast channels: absorption, refraction and dark-field are accessible using ABI (also known as Diffraction Enhanced Imaging (DEI)). As seen in Fig. 3, the technique uses a crystal analyser placed between the sample and detector, which modulates the beam's intensity as a function of the angle of incidence. If the crystal is rotated in the beam in a stepped manner and the intensity per step recorded, the *rocking curve* can be obtained. At a certain angle, maximum intensity will be measured, and this is known as the Bragg angle. [12]

Commonly, two images are obtained, one on either side of the rocking curve, allowing to separate the absorption and refraction signals. A third image is required to isolate the dark-field signal.

In ABI, precise alignment of the crystal is necessary. It is generally performed at synchrotrons for its monochromatic and highly collimated beams. While technically a monochromator can be used with a lab-source, in practice this reduces the flux to a level where there are too few photons to conduct a scan.

2.1.4 Grating Interferometry (GI)

Grating interferometry, also known as Talbot-Lau, is based on the Talbot effect. That is, at specific distances from a periodic object illuminated by a monochromatic beam, images of the object will be replicated, called the self-imaging effect. The optical elements in the set-up are commonly known as “gratings” as opposed to “masks” in EI. As with ABI, GI provides attenuation, refraction and dark-field images, allowing multi-modal CT scans to be performed.

As shown in Fig. 4, two gratings are employed. The first (G1) shapes the wavefront in a certain way, with the pattern being replicated at the plane of the detector. A sample in the beam distorts that wavefront due to the attenuation, refraction, and scattering it induces. While in principle it is possible to detect those distortions directly, in practice detectors with pixels much larger than the local wavefront distortions are used. To visualise the distortions, GI relies on an analyser / absorption grating (G2) placed in front of the detector which converts the fringe positions into intensity signals. [10]

As this method relies on interference effects, a general requirement is a highly coherent and monochromatic beam. Variations of the technique include adding a third grating: this grating would be placed in front of the source and split the incoming beam into an array of individually coherent, but mutually incoherent sources. The motivation behind the additional grating is to adapt the method to low brilliance x-ray sources. [17] Experimentally, it has been shown that the requirement for monochromaticity can be somewhat relaxed, but fundamentally the Talbot effect imposes the gratings to be designed for a specific, monochromatic energy.

Another drawback to GI imaging is the time-consuming nature of the phase stepping procedure. Phase stepping involves taking multiple images with respect to different relative positions of both gratings over a grating period, enabling the construction of ‘intensity oscillations’ on a per-pixel basis – which is a plot of the average intensity as a function of displacement.

From the phases of intensity oscillations $\phi(x, y)$, the wave-front phase profile $\Phi(x, y)$ can be extracted by 1D integration, due to the relationship given by:

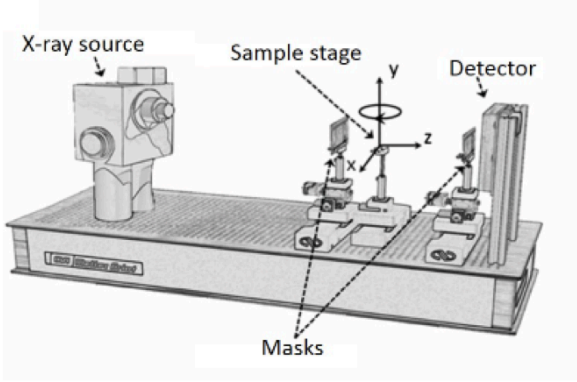
$$\phi = \frac{\lambda d \delta\Phi}{g_2 \delta x} \quad (4)$$

Where λ is the wavelength of the x-ray beam, d the distance between the gratings, and g_2 the period of the absorption grating downstream of the sample.

These intensity profiles can be used to extract absorption information too, as it contains the average signal per pixel with and without the sample in place. Fundamentally, that is the same as a traditional radiographic image taken without the interferometer (albeit with reduced flux), containing the attenuation coefficients. While the minimum number of required for a phase-stepping scan is 3 steps, 8 were taken in the following paper [18] rendering a small spider.

2.2 Edge-illumination

The following technique is the focus of my MPhil project.

XPCI technique	Schematic
Edge-illumination	 <p data-bbox="534 869 1385 987"><i>FIG 5 Edge-Illumination traditional set-up. From left-right: cone-beam x-ray source, sample mask, sample stage where the object would be placed, detector mask and finally the detector. Figure reproduced with permission of the rights holder, IOP Publishing [19]</i></p>

EI has been under continuous development within the Advanced X-ray Imaging group (AXIm) at UCL. It was first conceived by Olivo *et al* in the late 1990s [20] and consists of a relatively simple set-up: source, detector, sample stage with two additional masks upstream and downstream of the sample. It was initially demonstrated in synchrotron facilities but is mostly used in the laboratory nowadays, because the spatial coherence requirements of the source are relaxed.

The first (sample) mask – a periodic structure with alternating opaque and transmitting septa – splits the x-ray beam into an array of individual beamlets. The second (detector) mask, which is almost identical to the sample mask except distances are upscaled according to a geometric magnification factor, is placed immediately in front of the detector, in such a way that its opaque septa create insensitive regions between pixels. If an object is placed in the beamlets' path (usually immediately downstream of the sample mask), the measured intensity at a pixel will either increase or decrease, as a result of the beamlets undergoing attenuation, refraction and scattering.

At first glance, EI may seem schematically similar to GI but it does not rely on interference effects – it is a non-interferometric approach. Specifically, GI relies on beamlet interference and detection of local fringes, whereas in EI, the individual beamlets are observed. That makes EI naturally suited to non-microfocal lab sources which produce weakly coherent / incoherent radiation; furthermore, it has been demonstrated to have achromatic properties [21], that is, there is no preferential design energy to the system, in contrast to GI whereby the performance is strongly dependent on the x-ray spectrum. [22]

The premise behind the sample and detector mask in the set-up is that the relative displacement of these will cause the beamlets emerging from the first mask to either fall completely on an absorbing edge, the exposed pixel or somewhere in between. That correlates directly to the intensity measured by any given pixel – where total misalignment of masks results in minimum intensity recorded values and conversely total alignment gives rise to maximum values. The *illumination curve* (IC) is a plot of intensity vs. relative displacement (approximately Gaussian-shaped) where typically the values of intensity are normalised. Thus, by modifying the relative displacement of the sample and detector masks in the EI set-up, multiple frames can be taken at different relative mask positions, allowing to retrieve the IC on a pixel-by-pixel basis by fitting a suitable function (typically a Gaussian) to the acquired data. As noted in a topical overview [20], at least 2 frames on the IC are required to retrieve attenuation and refraction if the sample can be assumed to be non-scattering. Generally, when a sample is assumed to attenuate, refract, and scatter the beamlets, 3 or more frames on the IC are required. This can be thought of as obtaining 3 independent equations to solve for three unknowns.

The process of solving for the three unknowns, and thereby isolating three complementary images, is called “retrieval”. It is underpinned by the following observation: the presence of the object in the beam causes a reduction of the IC’s amplitude (due to attenuation), a shift of its centre (refraction) and broadening (scattering). Comparing those three parameters with and without the object permits the extraction of transmission, phase and dark-field images, respectively. Several ways of extracting those three images exist; for example, one may assume that the signal in neighbouring pixels are correlated, in which case it makes sense to fit three adjacent Gaussian profiles to the IC curves of three consecutive pixels. [23] Such approaches can provide greater robustness and detect smaller variations in the contrast channels compared to those methods where each pixel is fitted independently.

Although the merit of the EI technique has been proven through various experimental studies [24] [25], a key shortcoming lies in the use of the sample mask, which underpins the method’s working principle. As the mask blocks parts of the x-ray beams to generate the beamlet array, there are regions in the object which are not illuminated, i.e., for which no data are available in the projections. The width of those “gaps” is defined by the mask period. Consequently, without a process called *dithering*, the spatial resolution in the projections is limited by the mask period. Dithering is the process of stepping the sample laterally in sub-pixel steps relative to the sample mask to acquire consecutive frames, then intertwine these frames to obtain one complete (fully dithered) image.

In Fig. 5, the object would be placed on the sample stage; it would be displaced along the x direction for dithering and rotated around the y axis to cover the full 360° worth of projections when conducting a CT scan.

While it is easily feasible to apply dithering in planar EI scans, in a CT scan the sample must be stepped at each rotation angle. Thus, dithering involves the acquisition of several (e.g., 8) frames per angle, which is in addition to the 2, 3 or more frames to be acquired for different IC positions (much like the phase stepping procedure in GI). Considering that a typical CT scan involves taking data for 900-2500 rotation angles, it is evident that the number of frames that need to be collected (with exposure times on the order of seconds in a lab setting) rapidly becomes excessive. This is exacerbated by the fact that dithered scans with multiple IC

positions are bound to be step-and-shoot scans. In those scans, frames are collected when the sample is in a fixed position, and the sample is moved to the next position (dithering step, IC position, rotation angle) between frames. Step-and-shoot scans incur overheads which are significant, e.g., they can be on the scale of the exposure time or even exceed it.

3. Literature review

There are a number of different experimental approaches to XPCI, as alluded in the previous section. In the following, I am describing the key papers by the AXIm group that have direct relevance to the topic of this thesis.

3.1 Multi-modal CT with Edge-illumination

As explained in Sec. 2.2, EI is a method for performing multi-modal micro-CT scans; it is the principal research area of UCL's AXIm group. The ability to obtaining three contrast channels (attenuation, refraction and scattering) with EI was first demonstrated in 2014 [24]. A later paper demonstrated the compatibility of three-modal EI with polychromatic radiation, by retrieving multi-modal images from data obtained with a broad spectrum of x-ray energies. [21] As described in Sec. 2.2, three-modal signals are retrieved by taking sufficient measurements to plot the illumination curves, with and without the sample, on a pixel-by-pixel basis. The three-modal retrieval process is underpinned by the following model of the normalised intensity measured by a particular pixel with a sample in the setup:

$$\frac{I(x)}{I_0} = T[IC * S](x - \Delta x) \quad (4)$$

Where $I(x)$ is intensity recorded by that pixel, I_0 is the beam intensity incident on the sample mask, IC is the illumination curve *without the sample in place*, S is the scattering function which describes the ultra-small angle scattering of the beamlet induced by the sample, T is the transmission of the beamlet through the sample, and finally Δx represents the shift of the beamlet in the x direction due to refraction by the sample. Note that $(x - \Delta x)$ is the argument to the convolution between IC and S . In short, Eq. 4 states that the signal measured by a pixel is related to a broadening of the IC due to scattering, a shift caused by refraction and a reduced overall intensity due to attenuation. [26]

Eq. 4 models the intensity recorded at a particular pixel, for the relative displacement x between the sample and detector mask. This displacement needs to be varied when taking multiple frames on the illumination curve.

As mentioned in Sec. 2.2, in EI, the spatial resolution of multi-modal images is limited by the sample mask period in the first instance, which can however be increased if the signal is adequately sampled. In past investigations, that has been achieved by dithering, where the sample is scanned along the lateral direction with sub-pixel steps. If dithering is applied with sufficiently small steps, resolution would be at the scale of the beamlets, which is defined by the aperture width. The effect of dithering on resolution in EI CT was investigated experimentally by scanning deceased mice [27]. The paper provides a comparison between aperture-driven (accessed via dithered scans) and period-driven resolution (accessed through non-dithered scans). The spatial resolution for the different imaging scenarios schemes were

measured from the images. The results confirmed dithered images have a higher resolution than non-dithered ones.

3.2 Beam tracking CT

In traditional EI, the purpose of the detector mask is to impose absorbing edges in front of the detector, which introduce a sharp “cut-off” between pixels. As a result, the pixel response function is artificially sharper, leading to greater refraction sensitivity than if the detector edge was not available, particularly in the case of non-ideal, standard detectors. However, if instead a high-resolution detector is employed in the experimental design, then changes in the beamlets can be tracked without the detector mask. [28] [29] [30] The beamlets are resolved by the high-resolution detector, which allows to “see” the beamlets’ amplitude reduction, shift and broadening directly.

The technique of using a high-resolution detector to track beamlet changes is called *beam-tracking*. The benefits include a simplified experimental set-up, reduced exposure time and dose (as none of the radiation that has passed through the object is stopped by any opaque mask septa before reaching the detector). Moreover, multiple exposures on the IC need not be taken, which reduces long scan times.

It is worth noting that Shack-Hartmann sensors, which have been developed separately but bear resemblance to beam-tracking, consists of an array of “lenslets” on a mask to isolate a much larger beam into beamlets. [31] Each emerging beamlet will have a specific spot on the detector – and as with EI / beam-tracking – it is attenuated, displaced, or broadened because of a sample in the experimental set-up. Unlike EI / beam-tracking (at least in their classical implementation where the beamlets are long and narrow; current work investigates the use of round beamlets, similar to pencil beams), the changes are typically modelled by a 2D Gaussian function rather than 1D, where the peak properties can be extracted for each beamlet and compared to the values extracted when a sample is not in place. [32]

3.3 Cycloidal CT

Dithering improves spatial resolution, but it is time-consuming. There are two alternatives to the situation: the first one is to simply not apply dithering – that is, to only rotate the sample in the beam as is done in conventional CT. However, resolution in the reconstructed CT images will then be limited to the sample mask period. Moreover, aliasing artefacts may occur as the projections suffer from being under-sampled.

The second approach is to apply Cycloidal CT. [26] This approach was developed to achieve similar high spatial resolution observed with dithering while also reducing scan times. Rather than an imaging technique, such as GI, ABI, EI etc., Cycloidal CT is in fact a sampling scheme that can be applied whenever the x-ray beam is structured into an array of physically separated beamlets. In brief, instead of scanning the sample in multiple steps across one sample mask period for each rotation angle, the sample is translated *simultaneously* with being rotated (about

the x- and y-axis in Fig. 6, respectively). This gives rise to the name *Cycloidal CT*, as the concurrent rotation and lateral movement of the sample stage generates a cycloidal pattern. The key feature of the method is that the “roto-translation” movement of the sample can be performed continuously, removing the overhead of stopping and starting the sample stage motors between images, thus leading to much more efficient scan times (as there is no longer a need to interrupt the rotation to perform the dithering steps). This is equivalent to saying that Cycloidal CT enables the implementation of fly scans.

Comparing Cycloidal CT to a dithered scan and a CT scan where the sample is only rotated (“rotation only” in the following), it is important to note that the cycloidal method results in the data space (“sinogram space”) being sampled according to a different pattern. This is illustrated in Fig. 7. Here, the fully dithered approach is the "gold standard", as it provides fully sampled sinograms from which high-resolution CT images can be reconstructed. It can also be seen that, among the non-dithered sampling schemes, the cycloidal method results in a more evenly distributed sinogram space compared to the rotation-only method. In both cases, the missing data points can be interpolated using a mathematical data recovery technique to approximate the full grid. However, early results have shown that the cycloidal layout of the sampled data provides a much better basis for restoring the missing data.

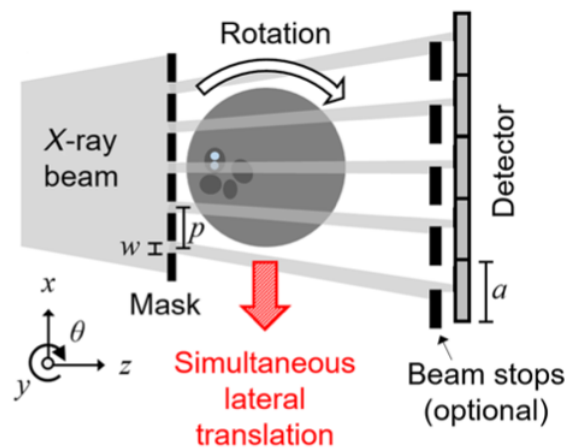


FIG 6 Schematic set-up of Cycloidal CT. The sample rotates about the y -axis and translates along the x -axis simultaneously. Figure reproduced from [33], licensed under the [Creative Commons Attribution 4.0 International License](https://creativecommons.org/licenses/by/4.0/)

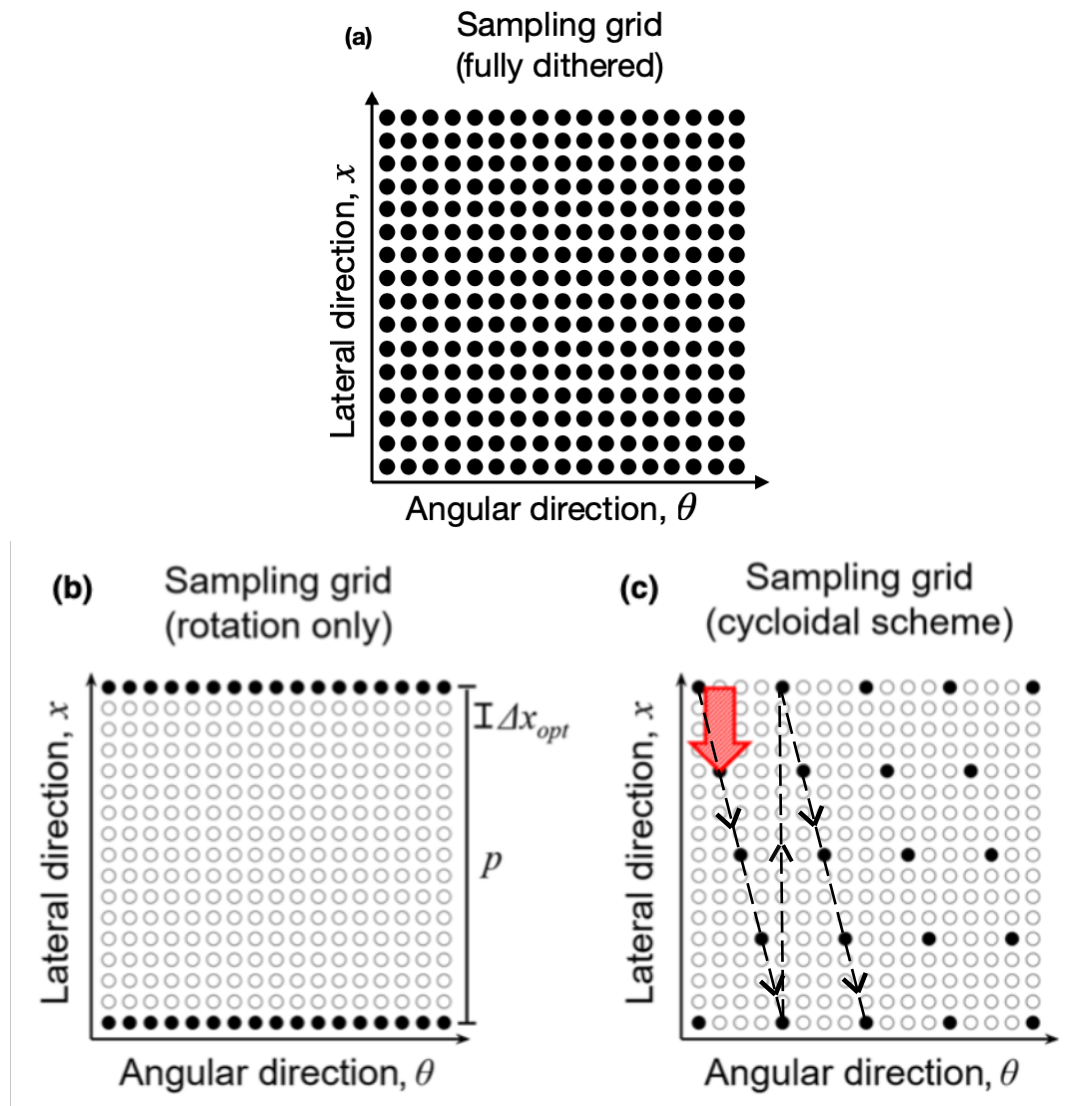


FIG 7 (a) The sinogram sampling grid when the gold-standard dithering, (b) the rotation-only, and (c) the cycloidal scheme is employed (dotted line indicates direction of scan). The black dots represent pixels that contain information and the empty dots missing information. The sinogram in the cycloidal scheme shows the pixels covered in a more evenly distributed fashion compared to the rotation-only scheme. Figure 7(b) and 7(b) reproduced from [33], licensed under the [Creative Commons Attribution 4.0 International License](https://creativecommons.org/licenses/by/4.0/)

In the first Cycloidal CT paper [33], the effect of the sampling scheme was demonstrated as a proof of concept on polyethylene spheres and rabbit oesophagus. Firstly, fully dithered (gold-standard) images were collected. Next, the rotation-only and cycloidal schemes were mimicked by sub-sampling the sinogram space according to the grids shown in Fig. 7b and 7c, and the “missing” entries on the sinogram were restored by applying bicubic interpolation such that the sinogram space as shown in Fig. 7a is restored. Following that, direct comparisons were made between the gold standard, cycloidal and rotation-only reconstructed slices. The results demonstrated that the spatial resolution of CT slices derived from the cycloidal scheme were comparable to the gold standard, while using only 1/8th of the data (and therefore dose) compared to the fully-dithered example. The dosage % level of the cycloidal sub-sampling was the same as that in rotation-only sub-sampling, yet rotation-only images were significantly blurrier.

While in [27] and subsequent publications Cycloidal CT was demonstrated for the attenuation and refraction contrast channels, it has not yet been applied to the dark-field channel.

4. Project: Altering an imaging system's resolution and contrast capabilities by means of x-ray absorbing masks

4.1 Introduction

The overarching goal is to demonstrate, experimentally, the effect of inserting one or two masks into an x-ray imaging system and to discuss the associated pros and cons, as well as future opportunities for masked-based set ups. My time in the AXIm group was spent on showing that by adding one mask (the sample mask) it is possible to increase the imaging system's resolution capabilities; by adding a second mask (the detector mask), it is possible to access multiple contrast channels and, thus, perform multi-modal CT. The analysis presented here is based on a rich EI CT dataset, consisting of fully dithered data for which several IC positions are available, acquired without masks entirely, with only a sample mask, and with a sample and detector mask. In addition, I have been investigating the effects of employing Cycloidal CT in the no mask/ one mask/ two mask scenarios.

4.2 Methods

4.2.1 Experimental system

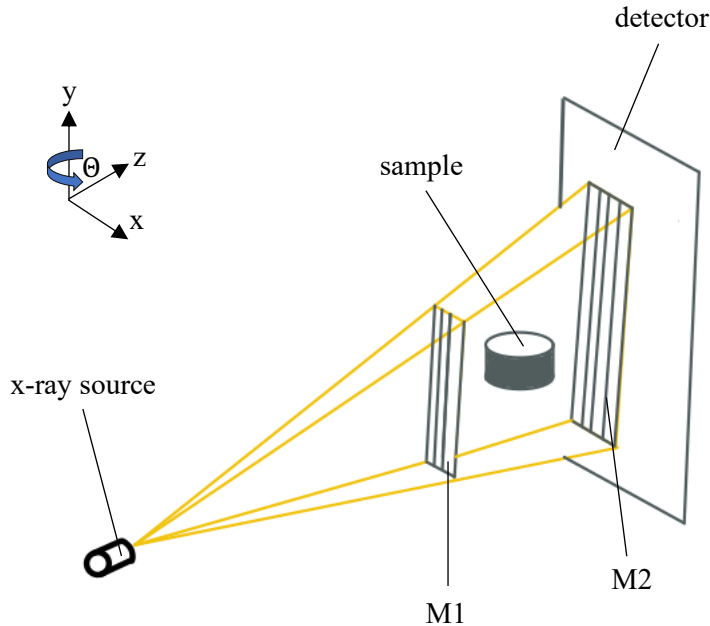


FIG 8 Schematic of imaging system – x-ray source is split into beamlets by the sample mask M1, and the detector mask M2, acts as an analyser to detect refraction of the beam. The sample is rotated about the y-axis and stepped along the x-axis. Figure reproduced from [34], licensed under the [Creative Commons Attribution 4.0 International License](https://creativecommons.org/licenses/by/4.0/)

Data were collected at X-Tek Systems-Nikon in Tring, Hertfordshire, UK. The experimental setup, a schematic of which is shown in Fig. 8, comprised a tungsten x-ray tube (X-Tek 160) with a focal spot of $80\mu\text{m}$. The detector is a dual-energy single photon counter with a Cd-Te CMOS sensor (XCounter XC-FLITE FX2) with 2048×128 square pixels with a size of $100\mu\text{m}$. Accounting for magnification, the pixel size at the sample mask is $75\mu\text{m}$. The source-mask distances M1 and M2 are 1.5m and 1.95m, respectively. [34].

Two masks were available for insertion into the system, both with nominal gold thickness of $300\mu\text{m}$. The sample mask had apertures of $20.83\mu\text{m}$ and a $75\mu\text{m}$ period; the detector mask had $28\mu\text{m}$ apertures and a $95\mu\text{m}$ period.

The object that was scanned with this system was a wooden pencil. Three sets of data were obtained: one set with no masks, another with just the sample mask, and finally both sample and detector mask. Each CT dataset was fully sampled with 4 dithering steps, 720 projections acquired over 360° and an exposure time of 1s per acquired frame. The source, which used a W target, was operated at 80 kVp. No filters were used in the dataset. Simulations performed for the same target and voltage estimates the mean energy to be about 40 keV. [35] Regrettably, the flux was not measured during the experiment, so an exact value cannot be given. In principle, however, the intensity at the sample without mask is 4x greater than with a mask in place (as the ratio between

transmitting and absorbing mask regions is 1/4). In practice, the intensity without the mask is slightly less than 4x that with the mask in place, as there is some transmission through the opaque septa (by the higher energy part of the spectrum). An explicit study into the repeatability of the translation stage (x-direction) has not been conducted, however the repeatability and accuracy requirement for the experiments discussed here are determined by the maximum spatial resolution that can be achieved, which is typically fulfilled for the type of motors used.

The scan in which two masks were used also included the acquisition of 5 frames for different positions on the IC, to enable the extraction of the three contrast channels: attenuation, refraction and dark-field. To process those data, the standard retrieval methods applied in previous literature [36] [21] were used. The process has been explained in Sec. 2.2 and 3.1. Briefly, two illumination curves were constructed, with and without the sample in place, for each pixel in the field of view. Approximating each curve to be Gaussian-shaped, the amplitude, mean and variance of the two curves were compared, each relating to the absorption, refraction and scattering coefficients respectively. Maps of the coefficients were constructed, thus leading to three separate projection images, one for each contrast channel. The same retrieval procedure was applied at all rotation angles. Consequently, 2D matrices of projection angle vs. pixel value were stitched together – forming sinograms. Finally, to reconstruct the absorption and scattering tomographic slices, the Filtered-back projection (FBP) algorithm (MATLAB's implementation of the inverse radon transform) was used on corresponding sinograms, and for refraction, the Hilbert transform was applied to the sinogram before back-projecting the data. The Hilbert transform combines the integration step with the ramp filter in the frequency domain – effectively, integration before back-projection does not need to be completed as separate steps to obtain the phase (δ) map, but rather together in a single step with the FBP. It should be noted that in FBP reconstruction, the customary assumption that x-rays travel in straight lines may seem contradictory to the observation that x-rays undergo refraction when passing through matter. At the same time, refraction angles are so small that x-rays remain contained within a single pixel, even when they are refracted. FBP back projects that information across a straight line limited to that pixel.

As the purpose of the described experiment was to demonstrate the effect that the masks in the system have on spatial resolution and contrast, the fully dithered images acquired without masks, one mask, and two masks were compared based on those metrics.

Spatial resolution was estimated based on profiles extracted across an edge within the pencil. A sigmoid function was fitted to the edge profiles to determine the edge spread function, before taking the derivative to obtain the line-spread function and measuring its full-width half maximum (FWHM). Python's packages NumPy and Matplotlib were used to process the data and plot the curves.

The contrast-noise-ratio (CNR) was estimated according to [37]:

$$CNR = \frac{I_S - I_B}{\sqrt{\frac{\sigma_S^2 + \sigma_B^2}{2}}} \quad (5)$$

Where I_S is the “signal” (i.e., average grey value in a homogeneous region of the sample), I_B is the average background grey value, and finally σ_S and σ_B are the standard deviations of the signal and background grey values, respectively. Small sections in the reconstructed images were chosen as the background and sample region of interest (ROI); the same areas were selected across all images for consistency.

To test the cycloidal sampling scheme and demonstrate its superior performance over a rotation-only scheme, the fully dithered sinograms were sub-sampled (i.e., data points removed from the grid) to mimic what would have been achieved if Cycloidal CT or rotation-only CT had been performed experimentally. When applying cycloidal sub-sampling, there are several ways of generating an interlaced grid like the one shown in Fig. 7c, as there are several options for the offset between the selected data points per rotation angle. The offset value is defined as the spacing between adjacent pixels in the x -direction; the red arrow in Fig. 7c indicates an offset value of 3, for example. As it was not initially clear how to choose the offset, I tested different values to determine the one that provides the best spatial resolution. In both the cycloidal and rotation-only sinograms, missing data points were recovered using MATLAB's implementation of bicubic interpolation.

4.3 Results

4.3.1 No masks vs one mask (fully dithered)

The tomographic images reconstructed from the data acquired without any mask and one mask (sample mask) are shown in Figs. 9 and 10, respectively. The images show axial cross sections through the pencil, revealing the graphite core inside a wooden holder that is surrounded by an outer layer of paint. Without a mask and with the sample mask only, the imaging system is only sensitive to attenuation contrast, hence this is the contrast shown in the images.

Upgrading the system set-up from no masks to only a sample mask improves the spatial resolution. If no mask is used, the imaging system resembles a conventional x-ray micro-CT scanner. In this case, at least in theory, the resolution in the images is driven by the characteristics of the x-ray source and the detector (“source-detector driven resolution”). An estimate of the system resolution, σ_{sys} , is $79\mu\text{m}$, calculated by taking into account the system magnification M , variances of the detector spatial resolution σ_{det}^2 and source distribution σ_{src}^2 using Eq. 6 [38]

$$\sigma_{\text{sys}}^2 \approx \left(1 - \frac{1}{M}\right)^2 \sigma_{\text{src}}^2 + \frac{1}{M^2} \sigma_{\text{det}}^2 \quad (6)$$

When adding the sample mask, the resolution in the images is driven by properties of the mask, either the period (if no dithering is applied) or the apertures (if dithering is applied).

Fig. 11 shows the LSF curves extracted from the images reconstructed without and with a sample mask. As expected, the LSF for the latter case is narrower, indicating that resolution is higher. The FWHM of those curves are $70.65 \pm 8.06\mu\text{m}$ and $20.55 \pm 0.17\mu\text{m}$, respectively.

While the above supports the hypothesis that an imaging system’s resolution properties can be altered by adding a sample mask into the system, by visual inspection of Fig. 9 and Fig. 10, the image taken without a mask appears provide a better visualisation of the small structures in the wood despite the lower resolution,. However, rather than being attributed to resolution, this is because Fig. 9 is less noisy than Fig. 10. This is caused by the fact that the mask blocks out substantial parts of the x-ray beam; hence, the sample is exposed to much fewer photons that can contribute to the formation of the image, leading to the x-ray statistics to be poorer and the image to be noisier. In this sense, a “fair” comparison of CNR is not possible here. To exclude this effect from my investigation (which is about spatial resolution and contrast), the data without the mask should have been acquired with a shorter exposure or an adequately reduced x-ray flux, such that the ultimate noise level is the same in the images acquired with no mask and with one mask.

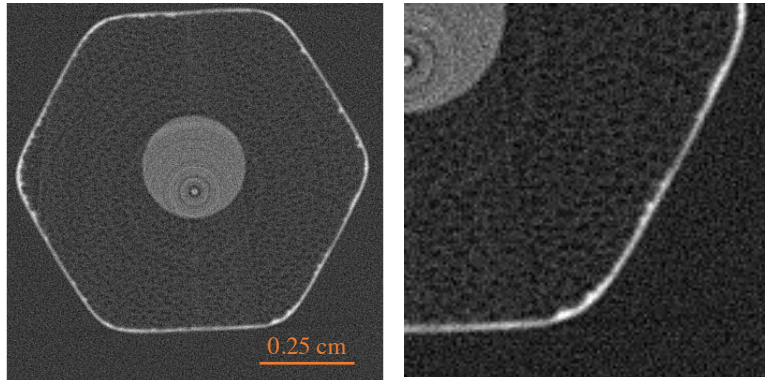


FIG 9 a) Reconstructed slice of fully dithered data and no masks in experimental set-up. The image shown is the attenuation slice of a wooden pencil, revealing the graphite core and outer layer of paint b) the axial slice zoomed in with adjusted contrast

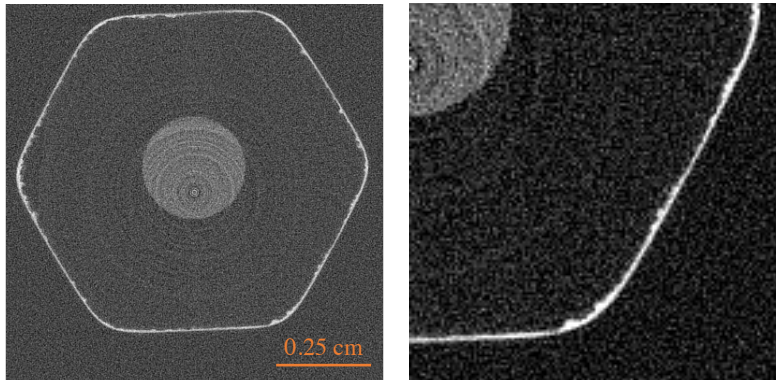


FIG 10 a) Reconstructed slice of fully dithered data and a single (sample) mask in experimental set-up. It is the same axial slice as in Fig. 9; the result is noisier but with improved spatial resolution b) the axial slice zoomed in with adjusted contrast

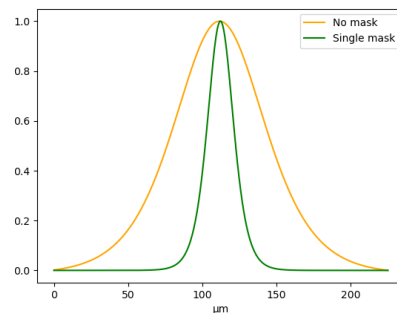


FIG 11 comparison of the LSF between 'no mask' and 'single mask' reconstructed slices. FWHM (μm): No mask – 70.65 ± 8.06 , Single mask – 20.55 ± 0.17

4.3.2 Two masks (fully dithered)

Extending to a double-mask set-up introduces the refraction and dark-field signals and therefore enables the extraction of multi-modal images. The expected benefit is twofold; first, refraction images are known to have a higher CNR than attenuation ones at the same dose level. Second, the dark-field channel provides additional information on the micro-structure of the sample.

The multi-modal tomographic images acquired with two masks in the setup are shown in Fig. 12. It is immediately obvious that the refraction image allows seeing the structure of the wood, while this is not possible in the attenuation image. The visible spots on the pencil are likely to be tracheids – long, tapered cells in softwood species including cedar wood, used to manufacture pencils. The wood of the refraction image can be compared to x-ray scans [39] of another type of softwood (pine), where the shape and length scales of tracheid cells can be seen. Since the images were extracted from the same raw data, in this case they were acquired with the same number of photons, hence a fair comparison of their CNR can be made. Based on Eq. 5 above, the CNR in the attenuation and refraction images was estimated to be 0.31 and 2.30 as seen from Table 1, respectively. The results support the idea that phase contrast CT enables higher quality reconstructed slices than absorption-based CT.

The dark-field image is clearly noisy and as such does not provide a significant CNR increase over the attenuation image. On the other hand, its purpose is to provide information on the object micro-structure that would otherwise not be available from the attenuation and refraction images alone, rather than increasing the CNR, and thus contribute to the richness of information that can be extracted from a scan with two masks. The system has a resolution of $\sim 20\mu\text{m}$, so scatterers smaller than this can be expected to contribute to the dark-field / scattering signal. That would fall under the USAXS (ultra-small angle x-ray scattering) range, rather than SAXS, which typically addresses length scales of 10-100nm. [40] In the particular case of the experiment discussed here, there seems to be little additional micro-structure revealed.

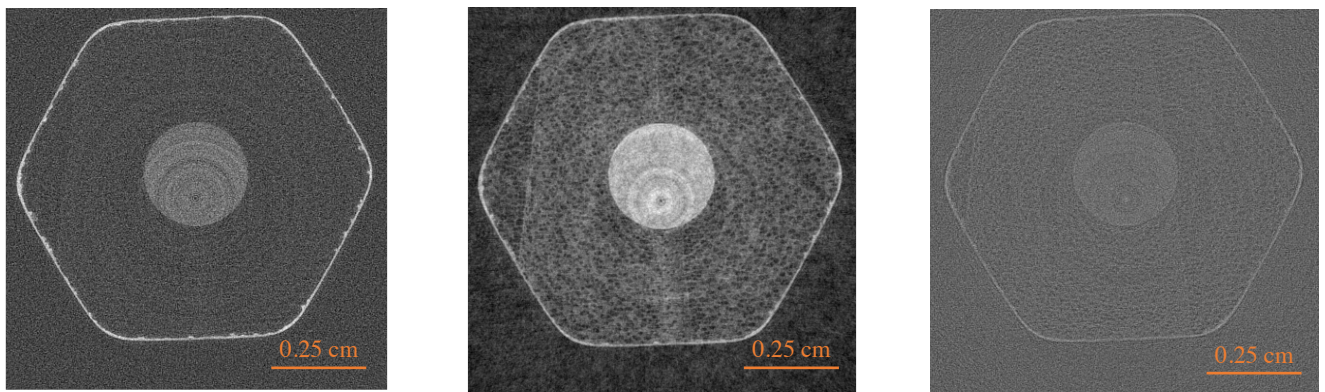


Table 1: Comparison of CNR values across reconstructed slices over fully dithered image in three contrast channels.

	Attenuation	Refraction	Scattering
Fully-dithered, double masks	0.31±0.04	2.30±0.22	0.26±0.03

4.3.3 Testing Cycloidal CT on the three contrast channels

The results of sub-sampling the dithered datasets in a cycloidal and rotation-only approach are shown in Fig. 13, 14 and 15 for the three contrast channels, respectively. In each figure, the top row shows the images obtained from Cycloidal CT when choosing different offset values. The bottom row shows the corresponding reconstructed rotation-only image. The resolution in those images was estimated based on the edge profile analysis described earlier. A plot of the LSF curves is also shown.

In all three channels, it is clear that the cycloidal scheme produces a blurrier image than the fully dithered equivalent. However, the cycloidal images are notably sharper than the rotation-only ones. Both observations are confirmed by the resolution estimates; these are $37.90\mu\text{m}$, $42.85\mu\text{m}$, $35.81\mu\text{m}$ for the cycloidal images, $66.24\mu\text{m}$, $82.89\mu\text{m}$, $69.43\mu\text{m}$ for the rotation-only images, while the dithered images have a resolution of $10.63\mu\text{m}$, $8.82\mu\text{m}$, $10.95\mu\text{m}$.

The optimal offset value for cycloidal sub-sampling is not conclusive. For the attenuation image, an offset of 3 pixels provides the highest resolution, for the refraction image this is the case for an offset of 1 pixel, and for the dark-field image the best resolution is achieved for an offset of 2. This outcome is not ideal, as the three contrast channels will ultimately be acquired with the same cycloidal acquisition using a fixed set of parameters. Further investigation is needed to understand whether the difference in “best” offset values stems from the analysis applied, or whether there is a true varying dependence on the offset between the contrast channels.

Attenuation

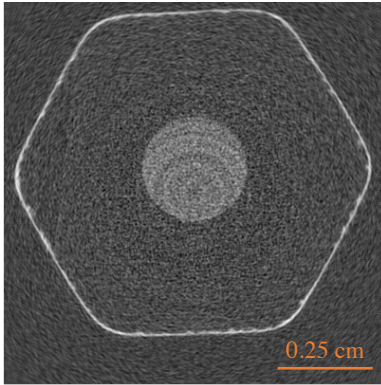
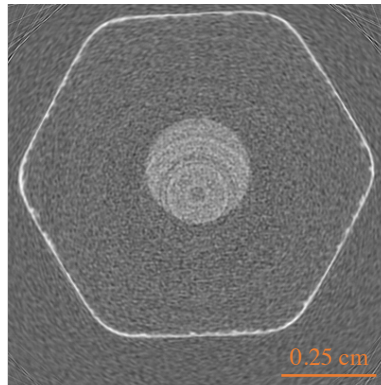
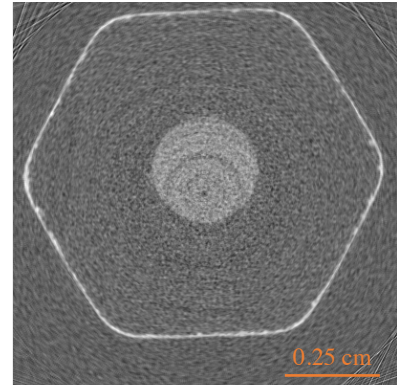


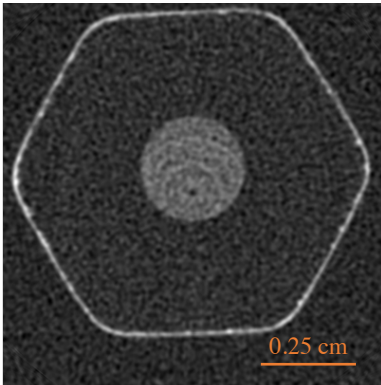
FIG 13 (a) interpolated – offset = 1



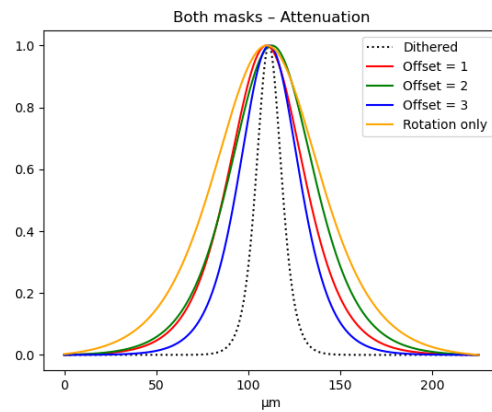
(b) interpolated – offset = 2



(c) interpolated – offset = 3



(d) rotation only



(e) comparison of the LSF between transmission reconstructions of fully dithered and interpolated data with varying offset values. FWHM (μm) : Dithered (reference) – 15.87 ± 0.23 , Interpolated offset 1 – 47.58 ± 2.70 , Interpolated offset 2 – 52.99 ± 7.80 , Interpolated offset 3 – 37.90 ± 4.84 , Rotation only – 66.24 ± 6.10

Refraction

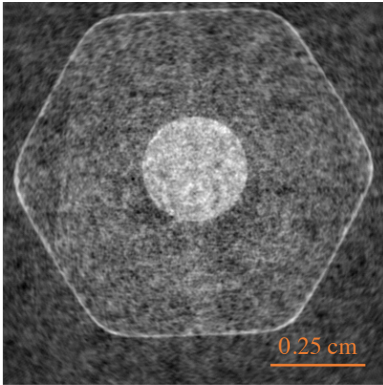
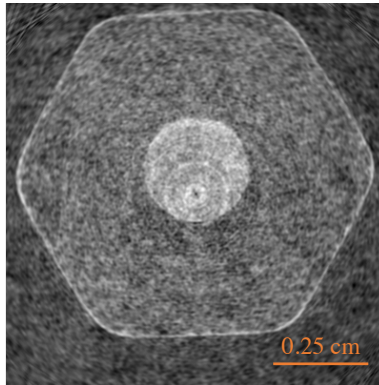
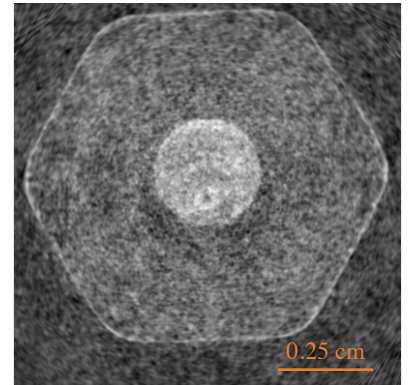


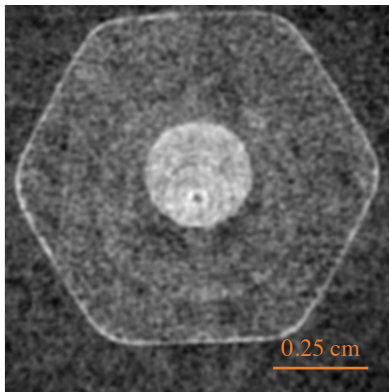
FIG 14 (a) interpolated – offset = 1



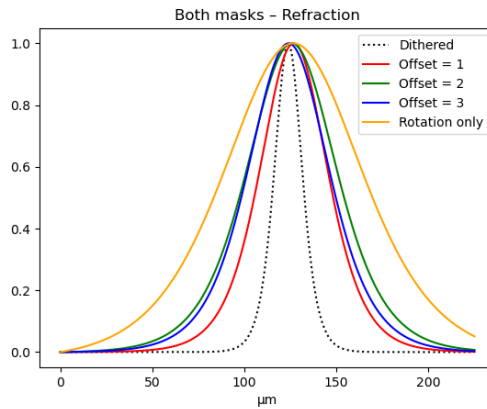
(b) interpolated – offset = 2



(c) interpolated – offset = 3



(d) rotation only



(e) comparison of the average LSF between refraction reconstructions of fully dithered, interpolated and rotation only data with varying offset values. FWHM (μm): Dithered (reference) – 17.64 ± 0.43 , Interpolated offset 1 – 42.85 ± 3.98 , Interpolated offset 2 – 56.62 ± 3.69 , Interpolated offset 3 – 51.26 ± 3.33 , Rotation only – 82.89 ± 4.78

Dark-field

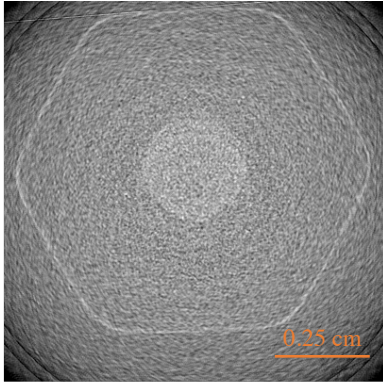
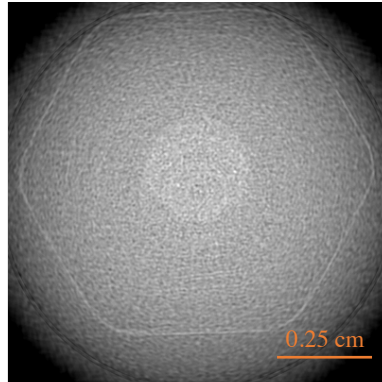
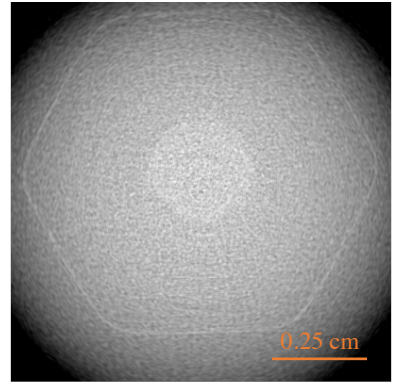


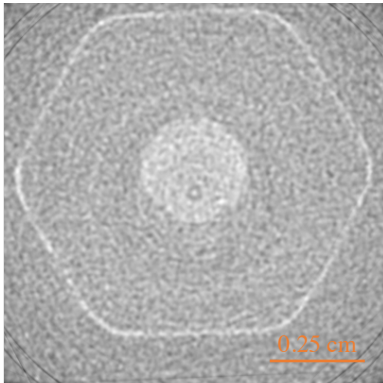
FIG 15 (a) interpolated – offset = 1



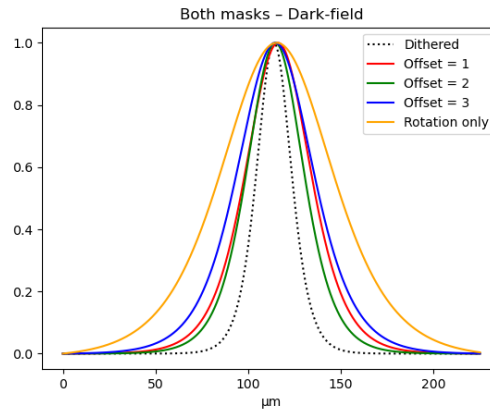
(b) interpolated – offset = 2



(c) interpolated – offset = 3



(d) rotation only



(e) comparison of the LSF between transmission reconstructions of fully dithered and interpolated data with varying offset values. FWHM (μm): Dithered (reference) – 21.90 ± 0.44 , Interpolated offset 1 – 40.78 ± 5.26 , Interpolated offset 2 – 35.81 ± 5.02 , Interpolated offset 3 – 47.75 ± 7.57 , Rotation only – 69.43 ± 7.67

4.4 Discussion

As verified with the experimental results discussed above, EI enables the reconstruction of high-resolution, multi-contrast CT images. Specifically, I have shown that the use of a single mask placed before the sample leads to a resolution increase compared to a no-mask setup, and the use of a second mask before the detector creates sensitivity to refraction and dark-field contrasts in addition to attenuation. This is a clear advantage of the method over conventional, attenuation based CT, and hence an opportunity to obtain better quality images for weakly attenuating samples that were traditionally considered difficult to image with x-rays.

Since EI does not rely on synchrotron radiation sources and has relaxed coherence requirements, it can readily be used in a laboratory setting. However, when using the technique in such settings, long scan times are typically needed. A single scan in the laboratory can take hours, often run as overnight scans. Two factors can be identified that limit the scanning speed of multi-modal, high-resolution scans using EI:

- (1) The need to acquire at least two frames on the IC to isolate the multiple contrast channels;
- (2) The need for dithering to achieve a resolution higher than that dictated by the sample mask period.

In CT, the number of frames that must be acquired to satisfy (1) and (2) is typically excessive. This is exacerbated by the fact that multi-modal, high-resolution scans cannot be implemented continuously but necessitate the use of step-and-shoot sequences, which incur overheads for stopping and starting the motors correspondingly.

Tackling this challenge is a primary focus of the AXIm group. In the following, I will give a brief account of past and current research aimed at speeding up high-resolution, multi-modal CT scans.

To begin with, Problem (1) can be addressed by replacing the full retrieval process by a simplified, approximation-based retrieval for which a single frame acquired on one of the IC slopes is sufficient. This method goes by the name of *single-shot phase retrieval* [41], and can be utilised to reconstruct hybrid images (containing a mixture of the phase and attenuation signal) with high CNR relative to traditional attenuation images. The primary assumption when using the retrieval method is that of a quasi-homogenous object, such that the ratio between the refractive index and absorption coefficient of the object is constant. The projected electron density can then be retrieved from a single input frame. [42] The advantage of the single-shot retrieval method is that it speeds up the acquisition of high CNR images. On the other hand, it is restricted to relatively homogeneous objects, and it only provides one hybrid contrast channel, rather than true multi-modality.

As an alternative, Problem (1) can be solved by changing the mechanism by which the beamlets' amplitude reduction, shift and broadening are detected. Beam-tracking was briefly described in Sec. 3.2: the beamlets are tracked directly by employing a high-resolution detector. As a result, the second (detector) mask is not needed, and gives rise to a simpler set-up than conventional EI.

Considering Problem (2), Cycloidal CT, introduced in detail in Sec. 3.3, could be a solution. The sampling scheme has been applied several times in past literature as well as this present study, with generally promising outcomes.

While high-resolution scans with mask-based systems were effectively bound to be step-and-shoot scans, Cycloidal CT could pave the way towards fly-scans – scans for which the sample continuously rotates and translates during acquisition. Fly-scans are arguably the fastest way of performing CT scans, as the overall scan time is determined by the exposure time alone (assuming that a detector with negligible read-out times is employed). The AXIm group’s strategy to perform fast, high-resolution, multi-contrast scans is to combine the “Beam Tracking” sensing mechanism with Cycloidal CT.

The overarching aim is to improve the method’s throughput capabilities, i.e. the ability to image as many samples as possible in a short time frames. In addition, the drive behind performing fly-scans is to move towards imaging dynamic samples (i.e., samples that change over time). This is enabled by having the scan time equal to the exposure time – higher temporal resolution can be achieved by reducing scan times which is facilitated by shorter exposures per frame. Shorter exposure times lead to higher noise, but recent progress in machine learning based denoising has provided previously unavailable options of handling noisy data. Furthermore, interest in reconstructing an image from sparse data sets (as would be the case with Cycloidal CT) is not a new phenomenon: Compressed Sensing, for example, is a powerful framework developed in 2004 by mathematicians from the United States. As most images in real-life have (or may be considered as having) limited information content (e.g., images have patterns and thus can be described from a small number of descriptors), compressed sensing allows to bypass Shannon-Nyquist’s theorem [43]. It has already been applied to a handful of undersampled MRI [44] and CT [45] scans. These powerful tools would open research to a wide range of interesting objects that we simply cannot image with traditional EI; for example, scanning dynamic objects that transform in a matter of minutes – which is clearly unachievable with the current EI approach, where a scan could last a couple of hours.

Some early experiments on combining Beam Tracking and Cycloidal CT have been performed in December 2021 at the Diamond Light Source Beamline I13-2 (Imaging Branch), conducted by myself and several other AXIm members. Data analysis is currently ongoing, but early results suggest that three-modal scans with a temporal resolution of < 12 s may be feasible.

Those datasets will be further analysed by the AXIm group in the forthcoming months, with a plan to submit another proposal for beam time at Diamond Light Source to push the temporal resolution even further, e.g. through the usage of very short exposure times and the application of the abovementioned denoising approaches.

5 Conclusion

In summary, this thesis has investigated the use of masks in x-ray CT setups and critically examined its merits and drawbacks. By comparing the effects of inserting one, or two, masks into an x-ray imaging system, I have shown that a single mask changes the resolution properties of the system, while two masks lead to reconstructed images with a higher CNR, as well as (at least in theory, via the dark-field channel) additional information on the object's micro-structure.

Further to that, I investigated whether Cycloidal CT, a sampling scheme designed especially for speeding up mask-based scans, can be applied to all three contrast channels. The results obtained (especially the ones on the dark-field channel, which were not available previously) suggest that three-modal fly-scans can indeed become reality. However, the finding that different offset values led to the best cycloidal results for the three channels requires further investigation. I have previously discussed the importance of faster scans and other techniques that can be used alongside cycloidal sampling schemes – namely a Beam-Tracking sensing mechanism or a “single-shot” phase retrieval when the sensing mechanism is EI. In this thesis, I have highlighted the combination of Beam Tracking and Cycloidal CT as a potential solution to the long scan times that have so far been incurred.

There are groups around the world who are working in tandem on other XCPI techniques. It is no surprise that research overlaps, and as briefly mentioned in the Literature section, Shack-Hartmann sensors share strong similarities with the Beam Tracking approach. Therefore, I believe that the findings described in this thesis, including on spatial resolution and Cycloidal CT, will be relevant to other groups and help to advance their approaches to XPCI.

Bibliography

- [1] F. Arfelli, M. Assante, V. Bonvicini, A. Bravin, G. Cantatore, E. Castelli, L. Dalla Palma, M. Di Michiel, R. Longo, A. Olivo, S. Pani, D. Pontoni, P. Poropat, M. Prest, A. Rashevsky, G. Tromba, A. Vacchi, E. Vallazza and F. Zanconati, "Low-dose phase contrast x-ray medical imaging," *Comunicación borrosa : sentido práctico del periodismo y de la ficción cinematográfica*, vol. 43, no. 10, pp. 2845-2852, 1998.
- [2] C. Urban, U. Straumann, U. Sennhauser, T. Luthi, R. Kaufmann, P. Schutz, C. Kottler, I. Jerjen and V. Revol, "Sub-pixel porosity revealed by x-ray scatter dark field imaging," *Journal of Applied Physics*, vol. 110, no. 4, p. 044192, 2011.
- [3] A. Olivo, K. Ignatyev, R. D. Speller and P. R. T. Munro, "Design and realization of a coded-aperture based X-ray phase contrast imaging for homeland security applications," *Nuclear instruments & methods in physics research*, vol. 610, no. 2, pp. 604-614, 2009.
- [4] P. Russo (Editor), "Basic Physical and Technological Aspects," in *Handbook of X-ray Imaging: Physics and Technology*, Florida, Taylor and Francis, 2017, p. 6.
- [5] J. Hsieh, "Computed Tomography: Principles, Design, Artefacts and Recent Advances, 2nd ed.," New Jersey & Washington, SPIE & Wiley, 2009, p. 42.
- [6] T. E. Gureyev, S. W. Wilkins, D. Gao, A. Pogany and A. W. Stevenson, "Phase-contrast imaging using polychromatic hard X-rays," *Nature*, vol. 384, no. 6607, pp. 335-338, 1996.
- [7] A. Bravin, P. Coan and P. Suortti, "X-ray phase-contrast imaging: from pre-clinical applications towards clinics," *Physics in Medicine and Biology*, vol. 58, no. 1, pp. R1-35, 2013.
- [8] A. Momose, "Phase-sensitive imaging and phase tomography using X-ray interferometers," *Optics Express*, vol. 11, no. 19, p. 2303, 2003.
- [9] M. Endrizzi, P. C. Diemoz, M. B. Szafraniec, C. K. Hagen, T. P. Millard, C. E. Zapata, P. R. T. Munro, K. Ignatyev, M. Marenzana, R. D. Speller and A. Olivo, "Edge illumination and coded-aperture X-ray phase-contrast imaging: increased sensitivity at synchrotrons and lab-based translations into medicine, biology and materials science," in *Proceedings of SPIE*, Florida, 2013.
- [10] T. Weitkamp, C. David, O. Bunk, J. Bruder, P. Cloetens and F. Pfeiffer, "X-ray phase radiography and tomography of soft tissue using grating interferometry," *European Journal of Radiology*, vol. 68, no. 3, pp. S13-S17, 2008.
- [11] U. Bonse and M. Hart, "An X-ray Interferometer," *Applied Physical Letters*, vol. 6, no. 8, pp. 155-156, 1965.
- [12] P. Russo (Editor), "Phase-Contrast X-ray Imaging and Other Aspects," in *Handbook of X-ray Imaging: Physics and Technology*, Florida, Taylor & Francis, 2018, p. 985.

- [13] A. Snigirev and I. Snigireva, "On the possibilities of x-ray phase contrast microimaging by coherent high-energy synchrotron radiation," *Review of Scientific Instruments*, vol. 66, no. 12, pp. 5486-5492, 1995.
- [14] S. C. Mayo, T. J. Davis, T. E. Gureyev, P. R. Miller, D. Paganin, A. Pogany, A. W. Stevenson and S. W. Wilkins, "X-ray phase-contrast microscopy and microtomography," *Optics Express*, vol. 11, no. 19, pp. 2289-2302, 2003.
- [15] D. H. Larsson, P. A. C. Takman, H. M. Hertz, U. Lundstrom and A. Burvall, "A 24 keV liquid-metal-jet x-ray source for biomedical applications," *Review of Scientific Instruments Online*, vol. 82, no. 12, p. 123701, 2011.
- [16] J. Hållstedt, E. Espes, U. Lundstrom and B. Hansson, "Liquid-metal-jet X-ray technology for nanoelectronics characterization and metrology," in *Advanced Semiconductor Manufacturing Conference*, New York, 2018.
- [17] F. Pfeiffer, T. Weitkamp, O. Bunk and C. David, "Phase retrieval and differential phase-contrast imaging with low-brilliance X-ray sources," *Nature Physics*, vol. 2, no. 4, pp. 258-261, 2006.
- [18] F. Pfeiffer, T. Weitkamp, A. Diaz, C. David, M. Stampanoni, P. Cloetens and E. Ziegler, "X-ray phase imaging with a grating interferometer," *Optics Express*, vol. 13, no. 16, p. 6296, 2005.
- [19] M. B. Szafraniec, T. P. Millard, K. Ignatyev, R. D. Speller and A. Olivo, "Proof-of-concept demonstration of edge-illumination x-ray phase contrast imaging combined with tomosynthesis," *Physics in Medicine & Biology*, vol. 59, no. 5, pp. N1-10, 2014.
- [20] A. Olivo, "Edge-illumination x-ray phase-contrast imaging," *Journal of Physics: Condensed Matter*, vol. 33, no. 36, p. 363002, 2021.
- [21] M. Endrizzi, F. A. Vittoria, G. Kallon, D. Basta, P. C. Diemoz, A. Vincenzi, P. Delogu, R. Bellazzini and A. Olivo, "An achromatic approach to phase-based multi-modal imaging with conventional X-ray sources," *Optics Express*, vol. 23, no. 12, p. 16473, 2015.
- [22] T. Thuring, W. C. Barber, Y. Seo, F. Alhassen, J. S. Iwaczyk and M. Stampanoni, "Energy resolved X-ray grating interferometry," *Applied Physics Letters*, vol. 102, no. 19, p. 191113, 2013.
- [23] C. Maughan Jones, M. Endrizzi, P. R. T. Munro, A. Olivo and F. A. Vittoria, "Retrieval of weak x-ray scattering using edge illumination," *Optics Letters*, vol. 43, no. 16, pp. 3874-3877, 2018.
- [24] M. Endrizzi and A. Olivo, "Absorption, refraction and scattering retrieval with an edge-illumination-based imaging setup," *Journal of Physics D: Applied Physics*, vol. 47, no. 50, p. 505102, 2014.
- [25] A. Olivo and E. Castelli, "X-ray phase contrast imaging: From synchrotrons to conventional sources," *La rivista del Nuovo cimento della Società Italiana di Fisica*, vol. 37, no. 9, pp. 467-508, 2014.

- [26] L. Massimi, "Laboratory-based x-ray phase contrast CT technology for clinical intra-operative specimen imaging," in *SPIE Medical Imaging*, San Deigo, California, 2019.
- [27] C. K. Hagen, M. Endrizzi, R. Towns, J. A. Meganck and A. Olivo, "A preliminary prnvestigation into the use of edge illumination x-ray phase contrast micro-CT for preclinical imaging," *Molecular Imaging and Biology*, vol. 22, no. 3, pp. 539-548, 2020.
- [28] I. K. Robinson, U. H. Wagner, P. C. Diemoz, M. Endrizzi and F. A. Vittoria, "Virtual edge illumination and one dimensional beam tracking for absorption, refraction, and scattering retrieval," *Applied Physics Letters*, vol. 104, no. 13, p. 134102, 2014.
- [29] I. Buchanan, A. Mittone, A. Bravin, P. C. Diemoz, M. Endrizzi and A. Olivo, "Simplified retrieval method for Edge Illumination X-ray phase contrast imaging allowing multi-modal imaging with fewer input frames," *Optics Express*, vol. 28, no. 8, pp. 11597-11608, 2020.
- [30] F. A. Vittoria, M. Endrizzi, P. C. Diemoz, A. Zamfir, U. H. Wagner, C. Rau, I. K. Robinson and A. Olivo, "X-ray absorption, phase and dark-field tomography through a beam tracking approach," *Scientific Reports*, vol. 5, no. 1, p. 16318, 2015.
- [31] A. Mikhaylov, S. Reich, M. Zakharova, R. Laptev, A. Plech and D. Kunka, "Shack-Hartmann wavefront sensors based on 2D refractive lens arrays and super-resolution multi-contrast X-ray imaging," *Journal of Synchrotron Radiation*, vol. 27, no. 3, pp. 788-795, 2020.
- [32] S. Reich, T. Dos Santos Rolo, D. Karpov, S. Gasilov, D. Kunka, E. Fohtung, T. Baumbach and A. Plech, "A Shack-Hartmann sensor for single-shot multi-contrast imaging with hard x-rays," *Applied Sciences*, vol. 8, no. 5, p. 737, 2018.
- [33] C. K. Hagen, A. Olivo, M. Endrizzi, O. Roche i Morgó and F. A. Vittoria, "Cycloidal computed tomography," *Physical Review Applied*, vol. 14, no. 1, 2020.
- [34] A. Astolfo, "Large field of view, fast and low dose multimodal phase-contrast imaging at high x-ray energy," *Scientific Reports*, vol. 7, no. 2187, 2017.
- [35] J. M. Boone and A. Seibert, "An accurate method for computer-generating tungsten anode x-ray spectra from 30 to 140 kV," *Medical Physics*, vol. 24, no. 11, pp. 1661-1670, 1997.
- [36] M. Endrizzi, A. Olivo, I. K. Robinson, R. D. Speller, J. L. Jones and T. P. Millard, "Hard X-ray dark-field imaging with incoherent sample illumination," *Applied Physics Letters*, vol. 104, no. 2, p. 024106, 2014.
- [37] M. Ghani, H. Liu, X. Wu, W. R. Chen, M. Kang, Y. Li and D. Wu, "Quantitative analysis of contrast to noise ratio using a phase contrast x-ray imaging prototype," in *Progress in biomedical optics and imaging*, San Fransisco, 2013.
- [38] S. W. Wilkins, Y. I. Nesterets, T. E. Gureyev, S. C. Mayo, A. Pogany and A. W. Stevenson, "On the evolution and relative merits of hard x-ray phase-contrast imaging methods," *Philosophical*

Transactions of the Royal Society A: Mathematical, Physical and Engineering Sciences, vol. 372, no. 2010, p. 20130021, 2014.

- [39] M. S. Moghaddam, J. Van den Bulcke, M. E.P. Wålinder, P. M. Claesson, J. Van Acker and A. Swerin, "Microstructure of chemically modified wood using X-ray computed tomography in relation to wetting properties," *Holzforschung*, vol. 71, no. 2, pp. 119-128, 2017.
- [40] J. Graetz, A. Balles, R. Hanke and S. Zabler, "Review and experimental verification of x-ray dark-field signal interpretations with respect to quantitative isotropic and anisotropic dark-field computed tomography," *Physics in Medicine & Biology*, vol. 65, no. 23, 2020.
- [41] P. C. Diemoz, F. A. Vittoria, C. K. Hagen, M. Endrizzi, P. Coan, A. Bravin, U. H. Wagner, C. Rau, I. K. Robinson and A. Olivo, "A single-image retrieval method for edge illumination X-ray phase-contrast imaging: application and noise analysis," *Physica medica*, vol. 32, no. 12, pp. 1759-1764, 2016.
- [42] P. C. Diemoz, F. A. Vittoria, C. K. Hagen, M. Endrizzi, P. Coan, E. Brun, U. H. Wagner, C. Rau, I. K. Robinson, A. Bravin and A. Olivo, "Single-image phase retrieval using an edge illumination X-ray phase-contrast imaging setup," *Journal of Synchrotron Radiation*, vol. 22, no. 4, pp. 1072-1077, 2015.
- [43] D. Mackenzie, "Compressed Sensing Makes Every Pixel Count," *What's Happening in the Mathematical Sciences*, vol. 7, pp. 114-127, 2009.
- [44] S. Geethanath, R. Reddy, S. A. Konar, S. Imam, R. Sundaresan, R. B. D. R and R. Venkatesan, "Compressed sensing MRI: a review," *Critical Reviews in Biomedical Engineering*, vol. 41, no. 3, pp. 183-204, 2013.
- [45] T. Mao, A. P. Cuadros, X. Ma, W. He, Q. Chen and G. R. Arce, "Fast optimization of coded apertures in X-ray computed tomography," *Optics Express*, vol. 26, no. 19, pp. 24461-24478, 2018.